# A Case Study on Tandem Configured Oscillating Foils in Shallow Water

Wendi Liu*

Department of Naval Architecture, Ocean and Marine Engineering
University of Strathclyde, Glasgow, G4 0LZ, UK

## ABSTRACT

**Previous research on the oscillating-foil turbine system has demonstrated its great potential for energy extraction. However, not much is known about the interaction of this device with its working environment. To determine the performance and environmental impact of an oscillating-foil turbine in shallow water, a case study have been conducted which was made of the dual oscillating energy extraction foils system with a tandem configuration which operates at two different water depths: i.e., $D$=5$c$ and $D$=10$c$. The performance and the environmental effects of the device were compared between shallow-water and deep-water cases. The results show a 10% efficiency loss in the $D$=5$c$ case compared with that of the deep water case, because of the interaction between the oscillating-foils and the seabed. It is also observed that the foil vortices dissipation rate of the $D$=5$c$ case is 13% less than that of the deep-water case due to the free-surface effect. The water level also rises 23% around the oscillating-foils location of the $D$=5$c$ case because of the blockage effect of the device.**

**Keywords: Oscillating-Foil Turbine; Shallow Water; Tandem Configuration; Renewable Energy.**

*Corresponding author. Tel: +44 141 5484371
E-mail address: wendi.liu@strath.ac.uk

## NOMENCLATURE

$A$ = sweep area of the oscillating foils ($m^2$)

$c$ = blade chord length (m)

$c_d(t)$ = instantaneous drag coefficient

$c_l(t)$ = instantaneous lift coefficient

$c_m(t)$ = instantaneous moment coefficient

$c_{op}$ = foil power coefficient

$c_{pit}$ = pitch centre of each foil from its leading edge (m)

$D$ = water depth measured from the free surface to the seabed in calm water (m)

$f^*$ = reduced frequency of oscillating foil

$f_0$ = foil oscillating frequency (Hz)

$h(t)$ = instantaneous heave of foil (m)

$h_0$ = foil heave amplitude (m)

$M$ = foil moment relative to the foil pitch centre (Nm)

$p_o$ = instantaneous power of the system (W)

$S$ = gap between the upstream and the downstream foil (m)

$t$ = instant time (s)

$T$ = oscillating period of the system (s)

$U_\infty$ = incoming flow velocity (m/s)

$V_t(t)$ = foil instantaneous resultant velocity (m/s)

$X$ = axis in horizontal (m)

$x_l o_l y_l$ = body-fitted coordinate

$Y$ = axis in vertical (m)

$\alpha(t)$ = foil instantaneous angle of attack (deg)

$\eta$ = system energy-extraction efficiency

$\theta(t)$ = instantaneous pitch of foil (deg)

$\theta_0$ = foil pitch amplitude (deg)

$\rho$ = fluid density ($kg/m^3$)

$\varphi$ = phase difference between heave and pitch of foil

$\psi$ = phase difference between upstream and downstream of foils

## 1. Introduction

The renewable-energy industry plays an important role in the energy field today. Research into renewable-energy devices accordingly provides key support for the renewable-energy industry, as it helps the industry overcome challenges and foresee opportunities. There are three general types of tidal/wind renewable-energy devices: horizontal axis turbine (HAT), vertical axis turbine (VAT) and oscillating-foil turbine (OFT). Compared with conventional turbines (i.e., HAT and VAT), the OFT is a novel device which requires more research to boost its commercialization process.

McKinney and DeLaurier first extracted wind energy in 1981 using the harmonically oscillating foil (McKinney and DeLaurier 1981). They designed a horizontally-aligned foil with a symmetrical aerofoil cross-section. McKinney and DeLaurier (1981) found that, with a prescribed combination of pitching and heaving motions, the output power and efficiency could be accomplished for both theoretical analyses of unsteady-foil aerodynamics and for wind-tunnel experimental tests.

Followed by McKinney and DeLaurier's work, many researchers studied the mechanism and energy extraction efficiency of the oscillating foil (Jones et al. 1997; Jones, Davids, and Platzer 1999; Davids 1999; Lindsey 2002; Jones, Lindsey, and Platzer 2003; Zhu 2011; Xiao et al. 2012; Campobasso and Drofelnik 2012; Liu, Xiao, and Cheng 2013; Le, Ko, and Byun 2013). Among the many researchers, Kinsey and Dumas (2008; 2011; 2012a, 2012b; 2014) carried out a series of studies on the oscillating-foil via experimental and numerical simulations recently.

Kinsey and Dumas (2008) carried out a detailed analysis of the mechanism of the energy-extraction type of oscillating foil. They report a maximum energy-extraction efficiency of 34% with reduced frequency between 0 and 0.25, a pitching amplitude between $0^0$ and $90^0$, a heave

amplitude of one chord length, a Reynolds number of 1100 and an NACA0015 foil shape. They also report that the energy-extraction efficiency is greater than 20% when the pitch amplitude is greater than $55^0$. Their results indicate that the heave amplitude and the oscillating frequency play a more significant role in energy-extraction performance than foil geometry plays.

Kinsey and Dumas (2012a) carried out a three-dimensional numerical calculation of the foil-oscillating turbine. They report that the hydrodynamic losses of the three-dimensional effect can be limited within 10% when endplates that use a foil tip with an aspect ratio larger than 10 are compared with the two-dimensional results. A non-horizontal hydrodynamic flow of up to $30^0$ with respect to the foil chord was also considered. They report that the energy-extraction performance is proportional to the projected energy flux.

Kinsey and Dumas (2012b) investigated two-dimensional, dual-oscillating foils with tandem configurations. Both of the foils could share the same flow stream under this arrangement to allow the oscillating foils to achieve their highest efficiency. Kinsey and Dumas report a beneficial effect from the interaction between the downstream vortex and the downstream foil which led to a total system efficiency of 64% under the optimized working condition. However, a harmful effect was also observed from the vortex-foil interaction, which leads the downstream foil to make a negative contribution to the system's energy-extraction efficiency. In comparison with the experimental results, the numerical simulations were over-predicted with respect to the peak-power coefficient. This may be because of the broken, two-dimensional coherence of the vortices in the three-dimensional experiments.

Kinsey and Dumas (2014) tested a single oscillating-foil turbine by using a two-dimensional, unsteady RANS solver. They report a maximum efficiency of 43% under a Reynolds number of 500,000. According to their results, better energy-extraction efficiency can be achieved when the effective angle of attack is around $33^0$. They also report that the leading-edge vortices

are not necessary around the best-performance region with high Reynolds number rather than the phenomenon at a low Reynolds number.

Most recently, Liu et al. (2016) designed a passive trailing-edge flexible oscillating foil for energy extraction by using a metal stiffener to control the stiffness of the trailing edge and a PDMS rubber to form the foil shape. They tested two types of material for the stiffener, which proves the beneficial effect of their passive trailing-edge flexible design on the energy-extraction efficiency of the oscillating-foil turbine. They also separately simulated and studied the Young's Modulus effect and the density-ratio effect of the stiffener by using virtual materials. Empirical equations that relate Young's modulus to energy-extraction efficiency were developed based on their study. The mechanism of this phenomenon was also investigated based on vortices analysis.

Most previous studies focus on the oscillating foil itself in terms of foil/motion optimization or the interaction of multiple foils. However, there has been little study of the interaction between the oscillating foil system and its working environment. The present case study investigates a tandemly arranged, dual oscillating-foils energy-extraction system which operates in shallow water. Two different water depths—i.e., five and 10 times foil chord length—are studied and compared with deep-water cases. The system performance, vortices structure and free-surface level are investigated under present working conditions.

Section 2 lists the problem description, mathematical formulations and numerical algorithms and validations/verifications of the present study. Section 3 presents results concerning energy-extraction performance in different water depth, vortices structure in near-foil and wake regions, free-surface level and flow trajectory. Finally, the conclusions of the study and suggestions for future work are summarised in Section 4.

## 2. Problem Formulation and Numerical Methodology

### 2.1.Problem description

The present case study considers a two-dimensional, tandemly arranged, oscillating-foils energy-harvesting system working in shallow water. A schematic plot on the oscillating-foils energy-harvesting system is shown in Figure 1. Please refer to Xiao and Zhu (2014) for the three-dimensional design of the oscillating-foils turbine. Since the present study is focusing on two-dimensional simulations of the oscillating-foils turbine, only 2D schematic diagram is presented herein. Two NACA0015 hydrofoils with a gap of $S$ and a chord length of $c$ were immersed and oscillated (combined with heave and pitch motion) in a uniform, viscous water flow with a velocity of $U_\infty$. The Reynolds number based on the foil chord length is $5\times10^5$. These foils pitch at $c_{pit}$ = 1/3 chord length, as measured from their leading edge. The oscillating-foils system is assumed to be bottom-seated. The distance between the foil and the seabed is keep changing during the operation of the system. In the present study, the closest distance from the pitch axis of the foil to the seabed is equal to one chord length, $c$, and the longest distance from the pitch axis of the foil to the seabed is one chord length plus two heave amplitude for all shallow water cases. Two water depths, $D$, which measure the distance from the free surface to the seabed in calm water were investigated: i.e., $D$=5$c$ and $D$=10$c$. Since the system is bottom-seated, different depths result in different distances from the system to the free surface, while the distance from the system to the seabed remains the same for all shallow water cases as mentioned above. A simulation of the oscillating-foils system under deep-water conditions—which assumes that the system is infinitely far from both the free surface and the seabed—was also carried out for comparative analysis. The incoming flow was simulated as calm water, which means no wave was generated from the inlet boundary.

**Kinematics for oscillating foils**

In the present study, the motion of the oscillating foils is simplified into a forced oscillating motion (McKinney and DeLaurier 1981; Jones et al. 1997; Jones, Lindsey, and Platzer 2003; Kinsey and Dumas 2008, 2012a, 2012b; Xiao et al. 2012) which is governed by the equations as follows:

$$h(t) = h_0 sin(2\pi f_0 t) \tag{1}$$

and

$$\theta(t) = \theta_0 sin(2\pi f_0 t + \varphi), \tag{2}$$

where $h(t)$ and $\theta(t)$ are the instantaneous heave and pitch motions. $h_0$ and $\theta_0$ are the amplitude of heave and pitch, respectively. $f_0$ is the oscillating frequency of the foil, and $\varphi$ is the phase difference between the heave and pitch motions. $t$ represents the instantaneous time.

The motion feature of a forced oscillating-foil turbine is determined by the pitch and heave motion. This is an ideal model for the OFT, which ignores the actuator effect. It is widely accepted and used by most OFT researchers, as it is simplified in mathematical formulae, but it can also provide useful insight into the physical phenomenon as a guideline of the industrial design (Xiao and Zhu 2014).

The oscillating reduced frequency $f^*$ is defined as follows:

$$f^* = \frac{f_0 c}{U_\infty}. \tag{3}$$

Following the work done by Kinsey and Dumas (2012b), $h_0$ and $\theta_0$ remains on $c$ and 70º, respectively; $\varphi$ has a fixed value of -π/2; the phase difference between the upstream foil and the downstream foil, $\psi$, is fixed as -π/2; the gap between two foils $S$ equals to 5.4$c$ and the reduced frequency $f^*$ equals to 0.14 for all cases in the present study. Thus, a high-energy-extraction efficiency could be achieved. This set of parameters was chosen since Kinsey and Dumas (2012b) has well studied the phenomenon and mechanism of the tandem arranged oscillating foils system under this condition. It is a good start point to investigate the shallow water effect to the system at present stage.

**Fluid force coefficients**

Several key parameters which quantify the energy-extraction performance of the tandem configured, oscillating-foils system are described below:

The foil-instantaneous lift coefficient $c_l(t)$ and foil-instantaneous drag coefficient $c_d(t)$ are defined as follows:

$$c_l(t) = \frac{instantaneous\ lift\ force}{\frac{1}{2}\rho U_\infty^2 c}, \tag{4}$$

and

$$c_d(t) = \frac{instantaneous\ drag\ force}{\frac{1}{2}\rho U_\infty^2 c}. \tag{5}$$

where, $\rho$ is the fluid density.

The foil-instantaneous moment coefficient $c_m(t)$ is defined as follows:

$$c_m(t) = \frac{M}{\frac{1}{2}\rho U_\infty^2 c^2}, \tag{6}$$

where $M$ is the foil-instantaneous moment relative to the foil pitch centre.

In this oscillating-foils model, the energy-extraction ability is measured based on the sum of the product of the lift force and the corresponding heave velocity with the product of the moment and corresponding pitch angular velocity. Thus, the non-dimensioned, instantaneous power coefficient $c_{op}$ is determined by,

$$c_{op} = \frac{p_o}{\frac{1}{2}\rho U_\infty^3 c} = \frac{1}{U_\infty}\left[c_l(t)\frac{dh(t)}{dt} + cc_m(t)\frac{d\theta(t)}{dt}\right], \tag{7}$$

where $p_o$ is the instantaneous power generated by the system.

The total energy-extraction efficiency $\eta$ is defined as,

$$\eta = \frac{\bar{p}_o}{\frac{1}{2}\rho U_\infty^3 A} = \overline{c_{op}}\frac{c}{A}, \tag{8}$$

where $A$ is the sweep area of the oscillating foils.

**Comparison among different turbines under body-fitted coordinate**

The three types of turbine (i.e., HAT, VAT and OFT) can operate based on foil/blade motions. A body-fitted coordinate $x_l o_l y_l$ is established for the turbine foil/blade. The original point of the body-fitted coordinate is fixed on the foil/blade centre line and 1/3 chord length from the

turbine foil/blade leading edge. The body-fitted coordinate is attached to the turbine foil/blade with corresponding heaving, rotating and/or pitching motions under the global coordinate. The foil/blade body-fitted coordinate $x_t o_t y_t$ and corresponding turbine foil/blade forces, resultant velocity $V_t(t)$ and angle of attack $\alpha(t)$ of the foil/blade are shown in Figure 2. With the help of the body-fitted coordinate, the three types of turbine with different configurations and working regimes can be compared with each other regarding the resultant foil/blade velocity and the foil/blade angle of attack, as shown in Figure 3. It is clear that the magnitude of the resultant velocity and foil/blade angle of attack for the HAT does not change during the turbine revolution. The magnitude of the resultant velocity and foil/blade angle of attack for the VAT varies as a sinusoidal function. There is one cycle for the $V_t(t)$ and $\alpha(t)$ during one turbine revolution and a $90^0$ phase difference between them. For the OFT, there are two sinusoidal cycles for the $V_t(t)$ during one turbine revolution. The $\alpha(t)$ of the OFT has one cycle during one turbine revolution, but the wave shape is not a sinusoidal function. The difference in performance of these three types of turbines is, thus, a result of the different behaviours of their $V_t(t)$ and $\alpha(t)$.

### 2.2.Mathematical formulations and numerical algorithm

The present simulations are performed by using the commercial CFD package ANSYS FLUENT 15.0, which is based on solving unsteady Reynolds-averaged Navier–Stokes equations (URANS). The governing equations for unsteady, incompressible flow associated with mass and moment conservation are as follows:

$$\rho \frac{\partial \boldsymbol{U}}{\partial t} = \boldsymbol{F_b} - \nabla \cdot p_\infty + \mu \nabla^2 \boldsymbol{U}, \tag{9}$$

and

$$\nabla \cdot \boldsymbol{U} = 0, \tag{10}$$

where $\boldsymbol{U}$ is the vector of velocity, $\boldsymbol{F_b}$ is the body force of the fluid, $p_\infty$ is the pressure and $\mu$ is the dynamic viscosity. A gravitational force with a gravitational acceleration of 9.81m/s$^2$ towards the negative direction of *Y*-axis applies to the entire calculation domain.

**Numerical issues**

The cases in the present study are simulated two-dimensionally within an isothermal fluid domain. The finite volume solver is calculated with second-order accuracy. The SIMPLE algorithm is used for the pressure-velocity coupling. To model the turbulence, the present research adopts a suggestion from Kinsey and Dumas (2012b) to use the one-equation Spalart-Allmaras turbulence model for simulations. The detailed turbulent model is governed by the following equation:

$$\frac{\partial}{\partial t}(\rho\tilde{\beta}) + \frac{\partial}{\partial x_i}(\rho\tilde{\beta}u_i) = G_\beta + \frac{1}{\sigma_{\tilde{\beta}}}\left\{\frac{\partial}{\partial x_j}\left[(\mu + \rho\tilde{\beta})\frac{\partial\tilde{\beta}}{\partial x_j}\right] + C_{b2}\rho\left(\frac{\partial\tilde{\beta}}{\partial x_j}\right)^2\right\} - Y_\beta + S_{\tilde{\beta}}, \tag{11}$$

where $\tilde{\beta}$ is the transported variable in the Spalart-Allmaras model, $G_\beta$ is the production of turbulent viscosity and $Y_\beta$ is the destruction of turbulent viscosity. $S_{\tilde{\beta}}$ is a user-defined source term, which is ignored in the present study. $\sigma_{\tilde{\beta}}$ and $C_{b2}$ are the constants of the Spalart-Allmaras turbulence model, which equal 0.667 and 0.622, respectively, as suggested by the ANSYS fluent theory guide (Fluent 2012b).

The volume-of-fluid (VOF) model is used to simulate and capture the motion of the free surface. The motion of the two oscillating foils is predetermined by a user-defined function

(UDF). The macro CG motion (Fluent 2012a) is adopted in the UDF code to control the oscillating (combined pitch and heave) motion. A spring smoothing and re-meshing function is used to maintain high-quality cells within the foils' motion. The instantaneous force and moment of each foil are calculated and saved at each time interval through UDF.

**Computational Domain**

The computational domain and boundary conditions are shown in Figure 4. The oscillating foils are set 25$c$ away from the inlet boundary and 75$c$ away from the outlet boundary. A uniform constant velocity in the $X$-axis direction is applied as the incoming flow for the inlet boundary condition as $u=U_\infty$, $v=0$ and $\partial p/\partial x=0$. A pressure outlet with $\partial p/\partial n=0$ is adopted for the outlet boundary. The bottom boundary is set as non-slip wall to reflect the seabed. As shown in Figure 4, the bottom seabed boundary (non-slip wall) extends for 25$c$ away from the oscillating foils system to the upstream, which is sufficient for the seabed boundary layer to be fully developed before interacting with the oscillating foils system. The top boundary is set as symmetry and the free surface is located horizontally between the top and bottom boundaries. For Shallow water cases (i.e. $D=5c$ and $D=10c$), the distance between the top and bottom boundaries of the calculation domain is 21$c$. In order to minimise the boundary effect, the top and bottom boundaries of the deep-water case are extended 150$c$ away from the oscillating foil system.

Since the re-meshing functions embedded in Fluent are used to handle the foils' motion, an unstructured grid is constructed within the foils' swapped regions, while structured-boundary layer grids are adopted for each of the foils to ensure the accuracy of the foil-forces calculation. A structured grid is used for the rest of the calculation domain to ensure an accurate and quick simulation, which is shown in Figure 5.

**2.3.Validations and verifications**

The computational methodology applied in the present study is validated with two cases against the published results. The first validation case is a pure heaving foil immersed in the water flow. A rigid foil with NACA0012 cross-section shape and chord length of $c$ heaving with a constant amplitude of 0.175$c$. The Reynolds number of the incoming flow that calculated based on the chord length of the foil is 20,000. The Garrick reduced frequency, $K_G$, is defined as $K_G=\pi fc/U$, where $f$ is the heaving frequency of the foil. Three $K_G$ were calculated by using the present simulation tool, which are 0.6, 1.6 and 2.8. The thrust coefficient of the foil is calculated as $Ct = 2Thrust/\rho U^2 c$. Quantitative comparison for the thrust coefficient of the foil with previous experimental results obtained by Heathcote et al. (2008) and numerical results obtained by Young (2005) were performed in Figure 6. There is a good agreement between present simulations and the previous experimental and numerical results.

Since the present study focus on the oscillating foil system, an additional validation case with tandemly configured oscillating foils was carried out and validated with Kinsey and Dumas (2012b). The Reynolds numbers of the incoming flow that calculated based on the chord length of the oscillating foil is 500,000. The reduced frequency, $f^*$, is equal to 0.14. The heave amplitude, $h_0$, and the pitch amplitude, $\theta_0$, are equal to chord length, $c$, and 70°, respectively. The distance between the upstream foil and the downstream foil is 5.4$c$. The oscillating phase difference between the two foils is 180°. The time histories of foils' lift and power coefficients for both present and published results are shown in Figure 7, and the corresponding vorticity contours are shown in Figure 8. In general, the calculated results compare well with the published results of Kinsey and Dumas (2012b), which prove the accuracy of calculation methods used herein to cope with the tandemly arranged oscillating-foils simulations.

Code verifications performed through the grid-dependence and time-step tests have been carried out to ensure the convergence of all simulations. The foils sub-zone, which is the key

zone to calculate the forces of foils, is extended from $X/c$=-5 to $X/c$=5 with a height of 4$c$. The cell numbers on the foils sub-zone is 94,806, which the power coefficient has a relative difference less than 0.1% when double the cell number within this sub-zone. The total cell numbers are 1,121,388 and 685,822 for deep-water case and shallow water case, respectively. After time step test, the time step size is chosen as $\Delta t = T/1000$. It is observed that the power coefficient has a relative difference less than 1% when half the time step size.

## 3. Results and Discussion

The performance of the tandemly arranged oscillating-foils system is analysed first in terms of its energy-harvesting ability in shallow water. A general presentation on the shallow water effect to the energy extraction efficiency and instantaneous forces of the oscillating foils system is shown in Section 3.1. The study is followed by an investigation of the vortices structure in near-foil and wake regions. A deeper analysis of the mechanism of the phenomenon observed in Section 3.1 is performed in Section 3.2 with the aid of flow field visualizations at different time instance and water depth. Finally, the level of the free-surface and flow trajectories in shallow water are presented.

### 3.1.Energy-extraction performance in different water depth

As presented in Section 2.1, the energy-extraction efficiency, $\eta$, is the criterion used to evaluate the performance of the oscillating foils in terms of their energy-absorbing ability. The energy-extraction efficiencies of the oscillating-foils system studied herein are illustrated in Figure 9 for different water depths. As mentioned above, the Reynolds number of results in Figure 9 is 500,000, which measured based on the foil chord length. The $h_0$ and $\theta_0$ remains on $c$ and 70º, respectively; $\varphi$ has a fixed value of -π/2; the phase difference between the upstream foil and the downstream foil, $\psi$, is fixed as -π/2; the gap between two foils, $S$, equals to 5.4$c$ and the reduced frequency, $f$*, equals to 0.14. The figure depicts upstream foil efficiency, downstream

foil efficiency and the efficiency of the total system. Compared with the deep-water case, the performance of the total system has a 10% and 9% decrease with $D$=5$c$ and $D$=10$c$, respectively. The total energy-extraction efficiency for $D$=5$c$ is slightly less than that for $D$=10$c$. This amount of energy loss is due to the free surface level difference and the seabed effect. The upstream foil lost more energy than the downstream foil.

In order to further analysis the performance of the system with different water-depth conditions, the instantaneous lift and power coefficients for both upstream and downstream foils are plotted in Figure 10. It is clear that, during one oscillating cycle, the shallow water reduces the peak lift coefficient of the upstream foil by about 17.9% and 24.7% for the downstream foil under the condition of $D$=5$c$. Less than 4% difference is observed for lift coefficient of the downstream foil between the case of $D$=5$c$ and that of $D$=10$c$, while less than 1% difference is observed for that of the upstream foils under the same condition.

As indicated by Xiao et al. (2012), the lift force makes a positive contribution to the power coefficient when it has the same sign as the heaving velocity, and vice versa. As can be observed in Figure 10 (a), from $t/T$=0 to $t/T$=0.4 and $t/T$=0.5 to $t/T$=0.6, the shallow-water condition reduces the absolute value of the lift of the upstream foil when both the lift and the heaving velocity of the upstream foil have the same sign. Thus, the instantaneous power coefficient of the shallow-water upstream foils is lower than that of the deep-water upstream foils during these times, which matches the observation from Figure 10 (c). During $t/T$=0.4 and $t/T$=0.5, the lift and heaving velocities of the upstream foils have an opposite sign, while the absolute value of lift for the upstream foil in shallow water is smaller than that in deep water. This results in an increment of the instantaneous power coefficient for the shallow water upstream foil compared with the deep water one of these time instances which also shown in Figure 10 (c).

For the downstream foils shown in Figure 10 (b), from $t/T$=0.2 to $t/T$=0.35 and from $t/T$=0.5 to $t/T$=0.75, the lift and heaving velocity have the same sign. The absolute value of lift for shallow-water downstream foils is larger than that for deep-water downstream foils during $t/T$=0.2 and $t/T$=0.35. On the other hand, the absolute value of lift for shallow-water downstream foils is smaller than that for deep-water downstream foils during $t/T$=0.5 and $t/T$=0.75. From $t/T$=0.45 to $t/T$=0.5 and from $t/T$=0.75 to $t/T$=1.0, the lift and heaving velocities of the downstream foils have positive signs. The absolute value of lift for shallow-water downstream foils is lower than that for deep-water downstream foils during $t/T$=0.45 and $t/T$=0.5, and it is larger during $t/T$=0.75 and $t/T$=1.0. From $t/T$=0.35 to $t/T$=0.45, the lift of the deep-water downstream foils has a sign opposite that of the heaving velocity, while the shallow-water downstream foils have the same sign. Based on Xiao et al. (2012), the shallow-water condition has a positive impact on the system performance of the downstream foil during $t/T$=0.2 and $t/T$=0.5. From $t/T$=0.5 to $t/T$=1.0, the shallow-water condition has a negative impact on the energy-extraction ability of the downstream foil. These observations coincide with that depicted in Figure 10 (c).

### 3.2.Vortices structure in near foil and wake regions

An analysis of the vortices structure in the near-foil and wake zones is carried out in this section to explain the energy-extraction performance observed in Section 3.1. The vortices in the near-foil zone have a direct impact on the foil forces. The upstream foil drops two types of vortices one after another, which are named UV1 and UV2 in this study. UV1 is the vortex in a counter-clockwise direction, while UV2 is the vortex in the clockwise direction. Similarly, the downstream foil drops two types of vortices, named DV1 and DV2, in a counter-clockwise and clockwise direction, respectively. The downstream foil has a strong and beneficial interaction with these vortices from the upstream foil, as indicted by Kinsey and Dumas (2012b). Since

the mechanism of the tandem arranged oscillating foils system under deep water condition has been well studied by Kinsey and Dumas (2012b), the present study only focuses on the water-depth effect on these vortices and their interactions with foils.

Figure 11 and Figure 12 show the vortices structure in the near-foil zone and the foil-wake zone at $t/T$=2/10 and $t/T$=7/10, respectively. At $t/T$=2/10, the upstream foil is in its up-stroke position near the bottom. The UV1 is still developing and is attached to the upstream foil. For the shallow-water cases (both $D$=5$c$ and $D$=10$c$), the UV1 in the near-foil zone has a strong interaction with the seabed and a vortex generated from the seabed, BV, with the counter-clockwise direction generated by this interaction in the seabed. Because of the exits of the seabed, the core vorticity of UV1 in the near-foil zone is 143 per second for $D=5c$ and 145 per second for $D=10c$, which are 11% and 9% smaller than that of the deep water case, respectively. The UV1 transfers a part of the dynamic energy to the seabed as the dynamic energy of BV. Boundary-layer separation of the upstream foil is also observed at this time instant, i.e., $t/T$=2/10. The integrated impact of the above reduces the lift-force generation of the upstream foil in $t/T$=2/10, as observed in Figure 10 (a).

At $t/T$=7/10, the upstream foil is in its down-stroke position and the UV2 is attached to the upstream foil. At this time, the seabed effect reduces and the free-surface effect increases due to the position of the upstream foil and UV2 shift upward towards the free surface. The difference in the vertical structure and the boundary layer of the upstream foil is limited between the shallow-water case and the deep-water case. Therefore, the lift-force generation of the upstream foil is similar in the shallow-water case and the deep-water case at this time, which is also coincident with Figure 10 (a). It indicates that the seabed has a stronger impact on the oscillating-foil energy-extraction than on that of the free surface at the present system configuration and working condition. The seabed influences the lift generated by affecting the

boundary layer and the counter-clockwise vortex of the oscillating foil when the foil is close to the seabed.

Figure 13 shows the velocity profile near the seabed boundary at the upstream foil location ($X/c$ = -2.7) and $D/c$ = 5. Both $t/T$=2/10 and $t/T$=7/10 are plotted and compared with pure seabed case (without oscillating foil). It can be seen that the boundary layer velocity profile of the seabed influenced by the motion of the upstream foil. At $t/T$=2/10 the seabed boundary layer is thinner than that of the pure seabed case. The velocity reduced instead of remaining a constant velocity as the pure seabed case in the inviscid region ($Y/C \geq 0.5$). It is because the upstream foil is close to the seabed and on its up-stroke position, the viscous region of the upstream foil boundary layer overlaps with that of the seabed boundary layer. At $t/T$=7/10, the velocity profile within the viscous region of the seabed boundary layer is same as that of the pure seabed case, but the velocity increases in the inviscid region because of the down-stroke motion of the upstream foil.

Similar to the upstream foil, the downstream foil sheds two reverse-rotating vortices: DV1 in the counter-clockwise direction and DV2 in the other direction. The structure and stress of DV1 and DV2 are dominated by UV1 and UV2. Unlike UV1, DV1 does not seem to exhibit dynamic energy transfer to the seabed. The downstream foil is at its down-stroke position at $t/T$=2/10 and is at the up-stroke position at $t/T$=7/10, which has a 180° phase difference with the upstream foil. UV2 and UV1 drop from the upstream foil and influence the downstream foil at $t/T$=2/10 and $t/T$=7/10, respectively. As observed by Kinsey and Dumas (2012b), these two configurations of the wake vortices and the downstream foil could enhance the local dynamic pressure to increase the energy-extraction efficiency at these times. It is clear from Figure 12 that the downstream foil in shallow water interacts with a weaker UV1 because of the seabed effect, which results in a performance reduction compared with that of the deep-water foil. As

indicated above, the vortex stress of the UV2 in shallow water is similar to that in the deep water, which leads to a similar performance of the downstream foil when it interacts with UV2 at $t/T$=2/10. As shown in Figure 11 and Figure 12, UV2 and UV1 separate into two parts after interaction with the downstream foil. The downstream foil passes through and fully interacts with one part of the vortex. The other part of the vortex sheds into the downstream without the blocking by the downstream foil.

The vortices shed from the duel oscillating foil system develop and move into the foil-wake zone. The structure and behaviour of these wake vortices are affected by the working environment. These wake vortices are necessary to study—especially for the application of oscillating foil system farm. Four vortices groups in the foil-wake zone are illustrated and marked out in Figure 11. As indicated above, a part of UV1 and UV2 move to the foil-wake zone after interacting with the downstream foil. In Vortices Group 1 of the deep-water case, it can be seen that the UV1 and UV2, together with the DV1 and DV2, form a four-core vortices system. As this four-core vortices system develops and moves downstream, it spreads into a larger space with a continuous decay of its vortices stress, as in Vortices Group 2, Vortices Group 3 and Vortices Group 4 of the deep-water case. Compared with that of the deep-water case, Vortices Group 1 of the shallow-water case contains one more counter-clockwise-rotated vortex, BV, and formed a five-core vortices system. Vortices UV2 and DV2 have a similar structure and stress for both shallow-water and deep-water cases. Because of the seabed, vortices UV1 and DV1 become flattened in the structure and weakened in the vortex stress. As the five-core vortices system moves downstream, UV1 dissipates quickly with the strong interaction of DV1 and BV, as shown in Vortices Group 2 of $D$=5$c$ and 10$c$. The vortices system of the shallow-water case spreads slowly compared with that of the deep-water case, because of the seabed and the free surface. The vorticity of DV1 in Vortices Group 4 of the $D$=5$c$ case is 25 per second, which is 19% stronger than that of the $D$=10$c$ case and 32%

stronger than that of the deep water case. The dissipation rate of DV1 measured from the Vortices Group 1 to Vortices Group 4 for the $D$=5$c$ case is 76%, while that for the $D$=10$c$ case and the deep water case are 82% and 89%, respectively. Therefore, the free surface has the effect to reduce the dissipation of the wake vortices. With this phenomenon, the intervals of the dual-foil system need to be 13% larger in the $D$=5$c$ case and 7% larger in the $D$=10$c$ case compared with that in deep water when these systems are installed as an array or energy farm, so as to ensure that the flow is sufficiently recovered at the downstream systems.

### 3.3.Free surface level and flow trajectory

As a renewable energy device, the influence of the oscillating foils system on the surrounding environment should be investigated, and minimised if possible, especially in the shallow water condition. The present study investigates the influence of the shallow water oscillating foils system to the free surface since the free surface level has a big influence on the performance of surface vessels. The flow trajectory around the oscillating foils system is also investigated in the present study as it has huge impacts to the nearby fish and under water plants. Figure 14 shows a snapshot of the phase contour for the shallow-water cases at $t/T$=2/10. It provides an overview of the wave generated by the oscillating foils. Figure 15 provides quantitative information about the free surface levels with different water depths. The blue zone in Figure 15 represents the location of the oscillating foils. For $D$=10$c$, the free surface level rises gradually from $X/c$=-20.00 to its peak value ($Y/c$=10.98) at $X/c$=6.40 and drops significantly to its bottom value ($Y/c$=9.39) at $X/c$=30.61. The free surface level, then, goes moderately up to the original level: i.e., 10$c$.

Unlike the $D$=10$c$ case, which has only one spick on its free surface level, the free surface level appears to have two spicks due to strong interaction with the oscillating foils. The free surface level reaches to the top of $X/c$=5.70 with the level of 6.16$c$, which is 23% higher than the calm

water level, and drops to the bottom at $X/c$=23.25 with the level of 3.42$c$. The free surface level goes back to 5$c$ with secondary small spicks and fluctuations after $X/c$=23.25. Under the present working condition, a shallower water depth results in a shorter distance (in terms of $X$-axis direction) between the free surface peak and valley, but it results in a larger difference (in terms of $Y$ axis direction) on the water level between the free surface peak and valley. With a shallower water depth, the free surface generates more waves with different wavelengths because the free surface is close to the oscillating foils.

In order to investigate the mechanism of the free surface changing, a velocity contour and a schematic plot for the flow trajectory for $D$=5$c$ at $t/T$=2/10 are presented in Figure 16 and Figure 17, respectively. From these two plots, the oscillating foils form a blockage zone by absorbing the kinetic energy of the water flow. The velocity of the stream of the water flow, which passes through the foils' swapped region, reduces rapidly and blocks the upstream flow. A certain amount of the water flow bypasses the blockage area by rising up to ensure the conservation of the mass flow rate as the high velocity flow bypass shown in Figure 17. A suction zone is also formed because of the blockage effect of the oscillating foils. The velocity of the flow stream reaches the lowest value at the junction of the two zones and gradually raises the velocity by interaction with the high-velocity flow in the bypass. The Karman vortices group, which was discussed previously and is dropped by the oscillating foils, is also formed and developed in this zone. The highest point of the free surface corresponds to the location of the lowest velocity of the flow stream at the zone junction, while the lowest point of the free surface is the boundary of the suction zone and the end of the high-velocity flow bypass, which is the location at which the high-velocity stream and the low-velocity stream mix. When the flow stream enters the blockage zone and reduces its velocity, the free surface level rises accordingly. When the flow stream passes the zone junction and increases its velocity, the free surface level drops and reaches the bottom level at the velocity-mixing location. The flow

streams recovers steadily after the velocity-mixing location, and the free surface level moderately rises back as discussed above.

## 4. Concluding Remarks

This study constitutes a case study of the dual oscillating energy-extraction foil system with tandem configuration, which operates in shallow water. Two different water depths have been studied: i.e., $D$=5$c$ and $D$=10$c$. Corresponding energy-extraction efficiency, vortices structures in the near foil/foil-wake zones and free surface level—all of which are influenced by the shallow water conditions—have been investigated.

The simulation shows that the efficiency of the system drops in the shallow-water condition compared with that in the deep-water condition. Furthermore, the simulation shows that the upstream foil loses more energy than the downstream foil when the dual-foils system operates in shallow water. The vortices-structure analysis shows a strong interaction between the boundary layer of the seabed and the upstream foil, which is believed to be the reason for the efficiency decrease. It is also observed that the vortices generated by the system spread and dissipate slowly in the shallow water due to the presence of the free surface, which has a higher impact on the downstream systems than in deep water. The free surface level is observed to increase in the near-foil zone because of the blockage effect of the dual-foils system. The free surface level drops back after the suction zone, according to the simulations.

Finally, the present study with two different depths of shallow water (i.e. $D$=5$c$ and $D$=10$c$) and one inter-foil spacing (i.e. $S$=5.4$c$) provides a start point of investigating the oscillating-foil energy-extraction turbine in shallow water. Further change the water depth and the inter-foil spacing may have novel observations/conclusions and are worth to investigate. These topics will be investigated in the follow-up studies in the near future. In reality, the boundary layer of the seabed usually complicated, especially when it has thick sediment and underwater

plants. In the present study, the seabed is simplified as a non-slip wall. The interaction between the oscillating foil system and the real seabed is also convolute but deserve to investigate in the future. The present study considers only one reduced frequency—i.e., $f^*$=0.14—which allows the system to have the best performance. The shallow water oscillating foils system at other reduced-frequency conditions need to be investigated in the near future. A three-dimensional test of the oscillating-foils system in shallow water must also be carried out in the near future.

## ACKNOWLEDGMENTS

Results were obtained using the EPSRC funded ARCHIE-WeSt High Performance Computer (www.archie-west.ac.uk). EPSRC grant no. EP/K000586/1.

## REFERENCES

Campobasso, M Sergio, and Jernej Drofelnik. 2012. 'Compressible Navier–Stokes analysis of an oscillating wing in a power-extraction regime using efficient low-speed preconditioning', *Computers & Fluids*, 67: 26-40.
Davids, Scott T. 1999. 'A computational and experimental investigation of a flutter generator', Monterey, California: Naval Postgraduate School.
Fluent, ANSYS®. 2012a. "Ansys Fluent UDF manual." In.: Release.
———. 2012b. 'Release 15, Theory Guide'.
Heathcote, Sam, Z Wang, and Ismet Gursul. 2008. 'Effect of spanwise flexibility on flapping wing propulsion', *Journal of fluids and Structures*, 24: 183-99.
Jones, K, M Platzer, K Jones, and M Platzer. 1997. "Numerical computation of flapping-wing propulsion and power extraction." In *35th Aerospace Sciences Meeting and Exhibit*, 826.
Jones, Kevin D, ST Davids, and Max F Platzer. 1999. "Oscillating-wing power generation." In *3rd ASME/JSME joint fluids engineering conference, San Francisco, CA*.
Jones, Kevin D, K Lindsey, and MF Platzer. 2003. 'An investigation of the fluid-structure interaction in an oscillating-wing micro-hydropower generator', *WIT Transactions on The Built Environment*, 71.
Kinsey, T, and G Dumas. 2014. 'Optimal operating parameters for an oscillating foil turbine at Reynolds number 500,000', *AIAA Journal*, 52: 1885-95.
Kinsey, T, G Dumas, G Lalande, J Ruel, A Mehut, P Viarouge, J Lemay, and Y Jean. 2011. 'Prototype testing of a hydrokinetic turbine based on oscillating hydrofoils', *Renewable Energy*, 36: 1710-18.
Kinsey, Thomas, and Guy Dumas. 2008. 'Parametric study of an oscillating airfoil in a power-extraction regime', *AIAA Journal*, 46: 1318-30.
———. 2012a. 'Computational fluid dynamics analysis of a hydrokinetic turbine based on oscillating hydrofoils', *Journal of fluids engineering*, 134: 021104.
———. 2012b. 'Optimal tandem configuration for oscillating-foils hydrokinetic turbine', *Journal of fluids engineering*, 134: 031103.

Le, Tuyen Quang, Jin Hwan Ko, and Doyoung Byun. 2013. 'Morphological effect of a scallop shell on a flapping-type tidal stream generator', *Bioinspiration & biomimetics*, 8: 036009.
Lindsey, Keon. 2002. "A feasibility study of oscillating-wing power generators." In.: DTIC Document.
Liu, Wendi, Qing Xiao, and Fai Cheng. 2013. 'A bio-inspired study on tidal energy extraction with flexible flapping wings', *Bioinspiration & biomimetics*, 8: 036011.
Liu, Wendi, Qing Xiao, and Qiang Zhu. 2016. 'Passive flexibility effect on oscillating foil energy harvester', *AIAA Journal*, 54: 1172-87.
McKinney, William, and James DeLaurier. 1981. 'Wingmill: an oscillating-wing windmill', *Journal of energy*, 5: 109-15.
Xiao, Qing, Wei Liao, Shuchi Yang, and Yan Peng. 2012. 'How motion trajectory affects energy extraction performance of a biomimic energy generator with an oscillating foil?', *Renewable Energy*, 37: 61-75.
Xiao, Qing, and Qiang Zhu. 2014. 'A review on flow energy harvesters based on flapping foils', *Journal of fluids and Structures*, 46: 174-91.
Young, John. 2005. *Numerical simulation of the unsteady aerodynamics of flapping airfoils* (University of New South Wales, Australian Defence Force Academy, School of Aerospace, Civil and Mechanical Engineering.).
Zhu, Qiang. 2011. 'Optimal frequency for flow energy harvesting of a flapping foil', *Journal of Fluid Mechanics*, 675: 495-517.

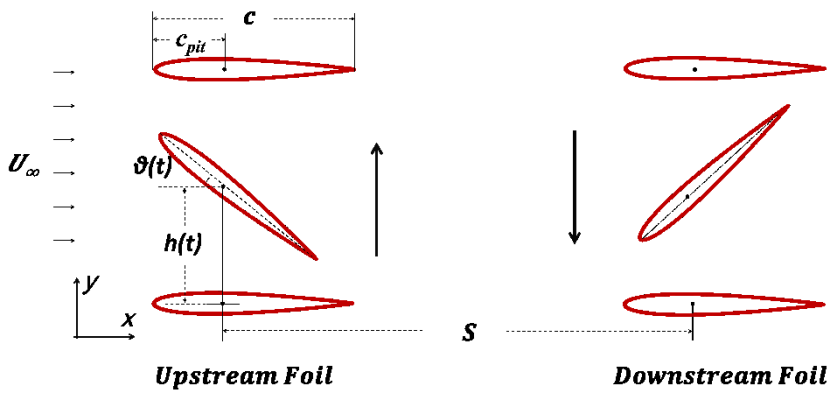


**Figure 1 Schematic diagram for oscillating energy extraction foils with tandem configuration.**

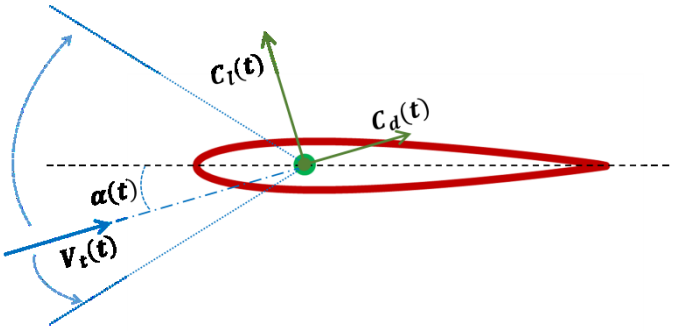


**Figure 2 Sketch of turbine foil/blade forces, resultant velocity and angle of attack under body-fitted coordinate $x_l o_l y_l$.**

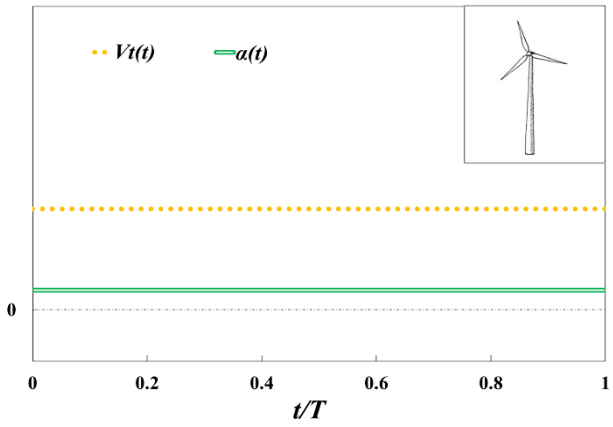


(a) Horizational Axis Turbine

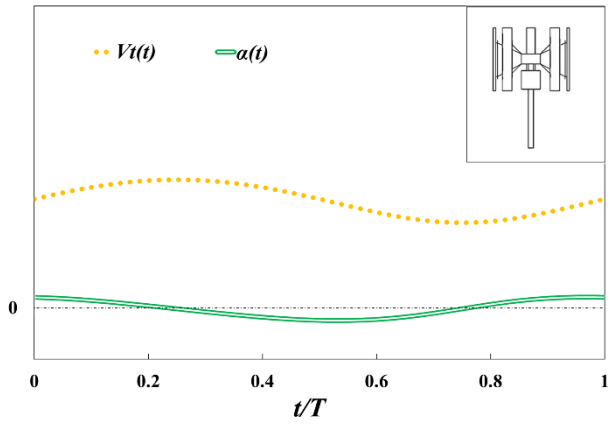


(b) Vertical Axis Turbine

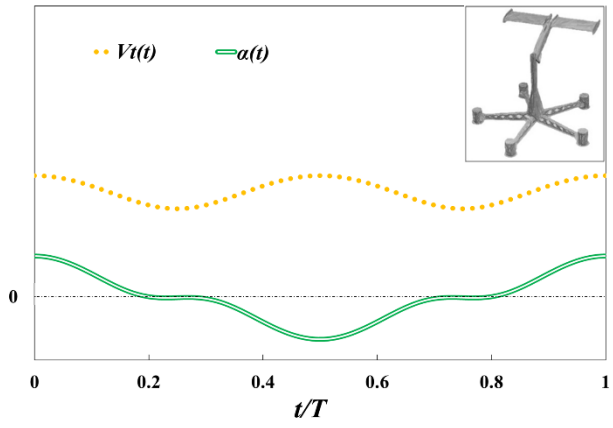


(c) Oscillating-Foil Turbine

**Figure 3 The schematic plot of instantaneous velocity and foil/blade angle of attack for the (a) Horizational Axis Turbine, (b) Vertical Axis Turbine and (c) Oscillating-Foil Turbine with a body-fitted coordinate $x_l o_l y_l$.**

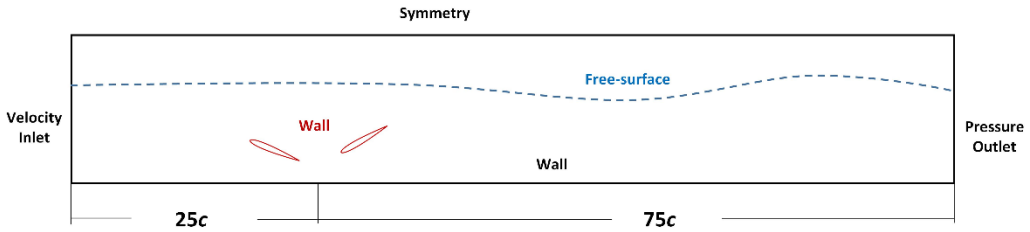


**Figure 4 Computational domain and boundary conditions.**

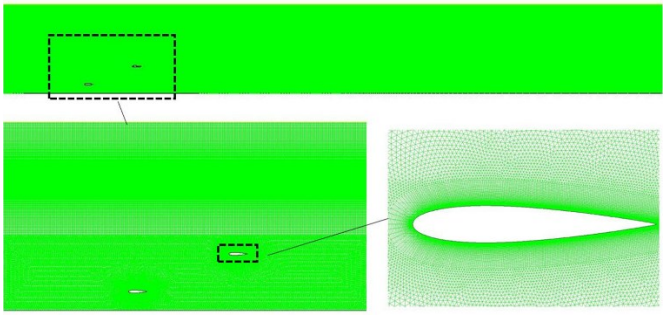

**Figure 5 Computational mesh details.**

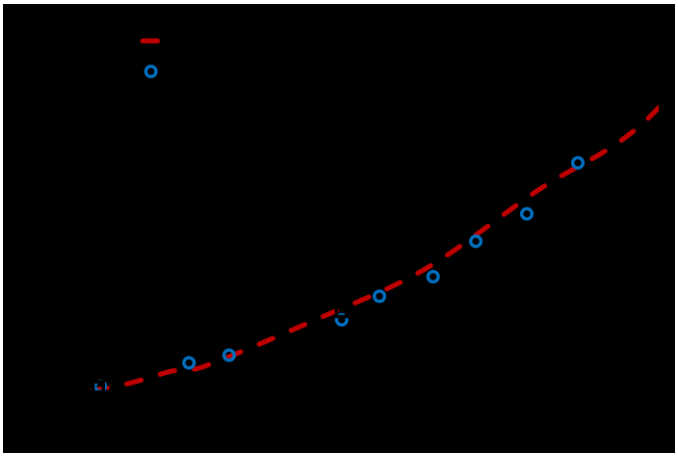

**Figure 6 Validation results on thrust coefficient for a rigid heaving foil with $Re$=2×10$^4$ and $h_0$=0.175$c$ which compared with numerical results from Young (2005) and experimental results from Heathcote et al. (2008).**

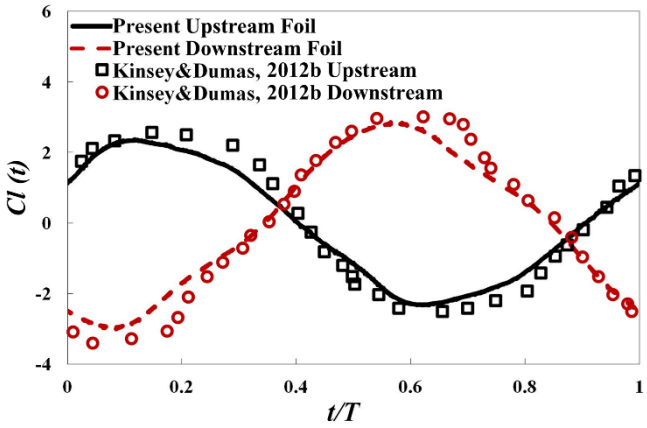


(a) Lift coefficient

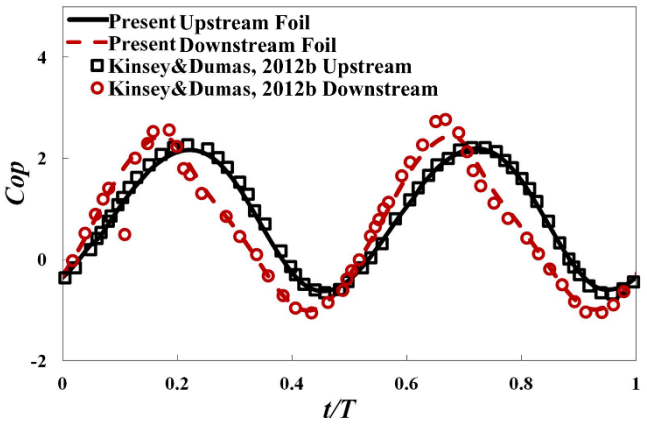


(b) Power coefficient

**Figure 7 Validation results on (a) Lift coefficient and (b) Power coefficient for tandem configured oscillating foils with $f^*$=0.14, $h_0$=$c$, $\theta_0$=70°, $S$=5.4$c$ and $\psi$=180° which compared with Kinsey & Dumas (2012b).**

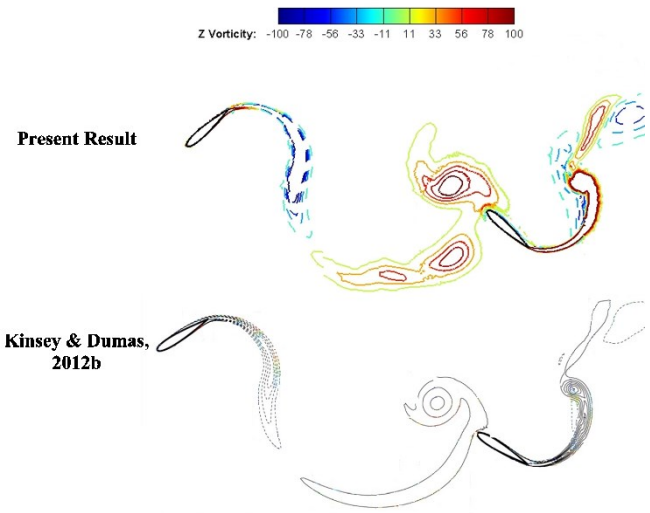


**Figure 8 Validation results on vorticity contour for tandem configured oscillating foils with $f^*$=0.14, $h_0$=$c$, $\theta_0$=70°, $S$=5.4c and $\psi$=180° which compared with Kinsey & Dumas (2012b).**

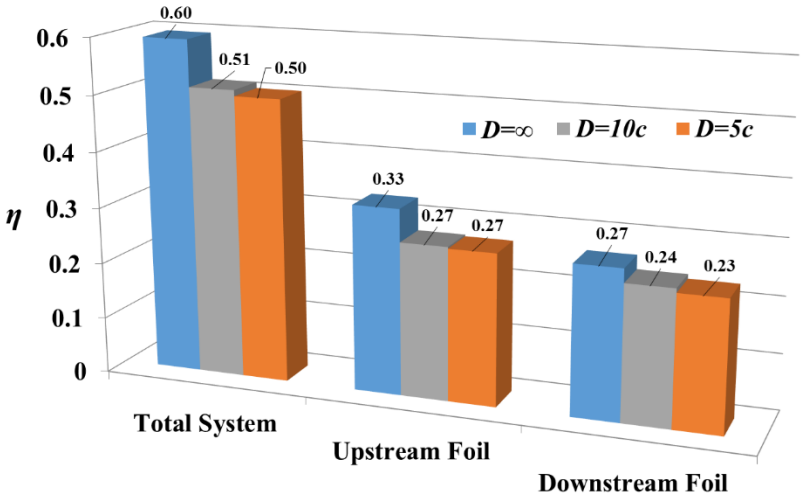


**Figure 9 The energy-extraction performance of tandem configured oscillating foils with different water depth.**

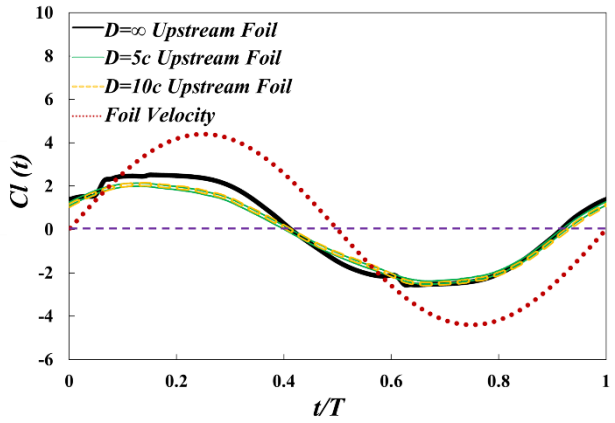


(a) Lift coefficient for upstream foil

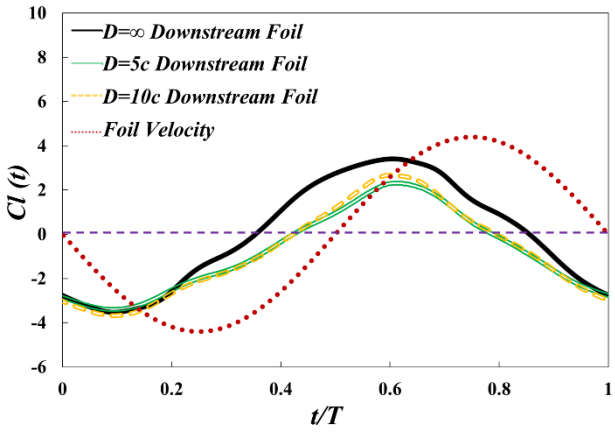


(b) Lift coefficient for downstream foil

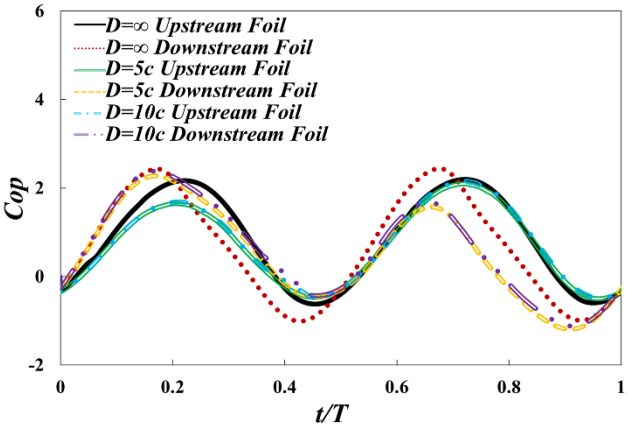


(c) Power coefficient

**Figure 10 Instantaneous results with different water depth on (a) Lift coefficient for upstream foil, (b) Lift coefficient for downstream foil and (c) Power coefficient.**

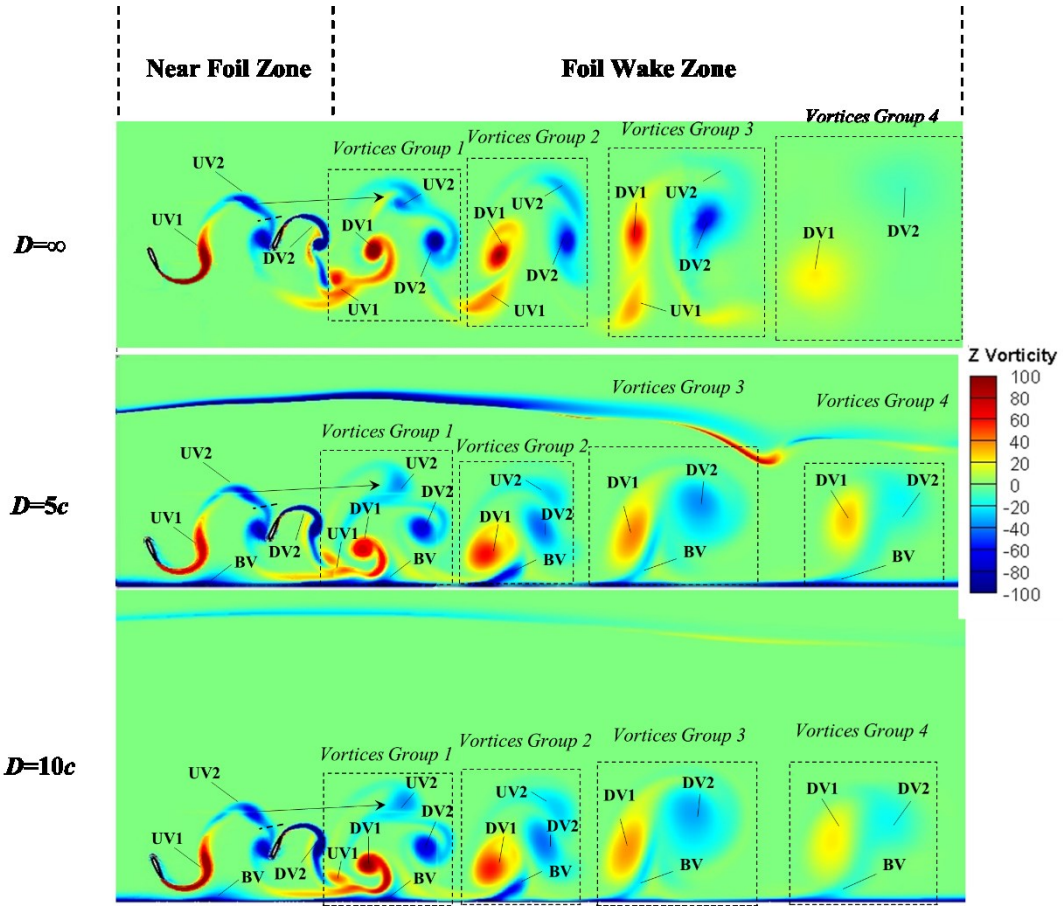


**Figure 11 Vortices structure with different water depth at *t*/*T*=2/10.**

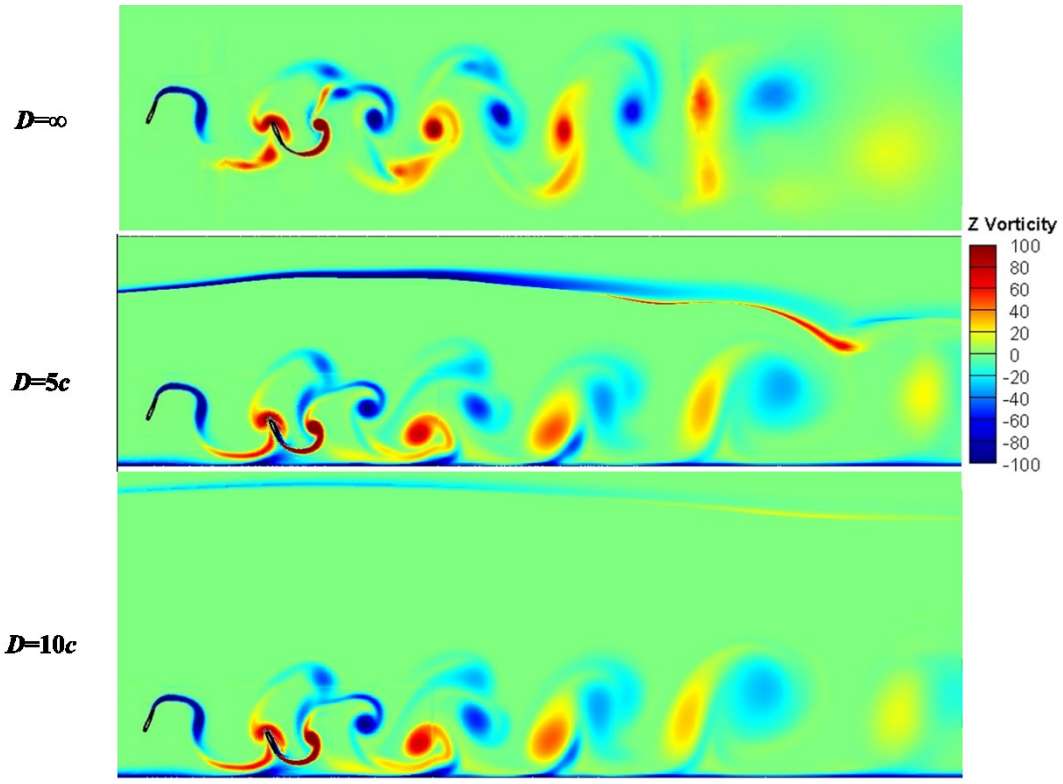


**Figure 12 Vortices structure with different water depth at *t*/*T*=7/10.**

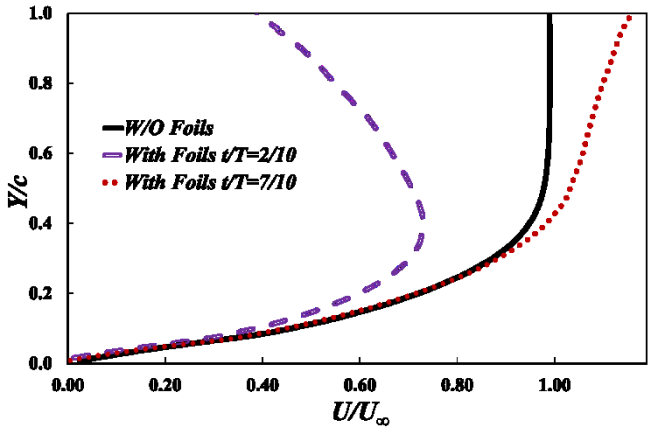


**Figure 13 Velocity profile near the seabed boundary with different time instance at *X/c* = -2.7 and *D/c* = 5 compared with flow pass seabed without oscillating foils.**

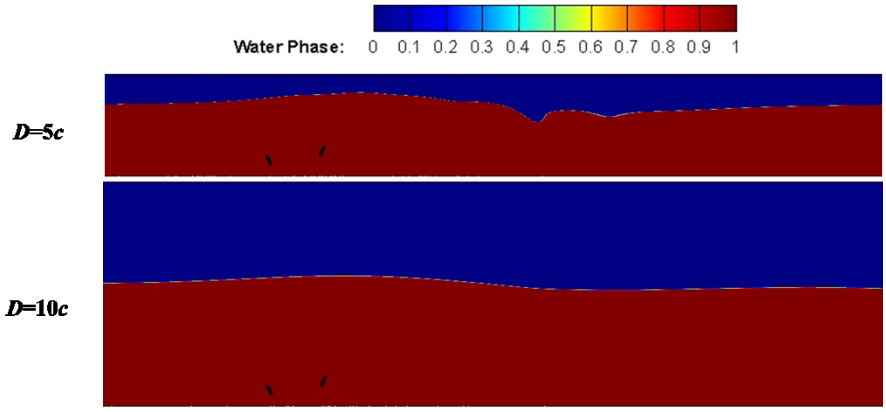


**Figure 14 Phase contour with different water depth at *t*/*T*=2/10.**

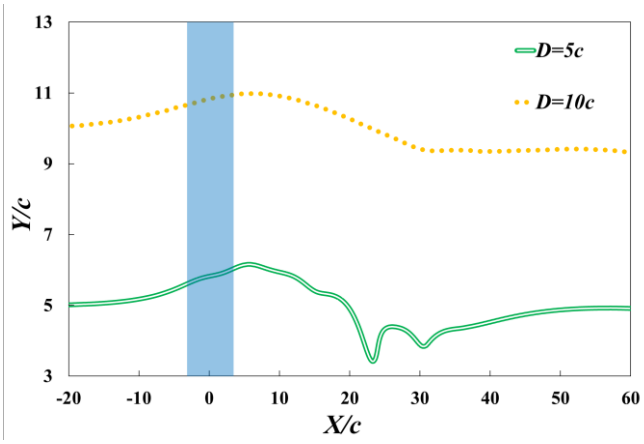


**Figure 15 Free surface level with different water depth at *t*/*T*=2/10. The blue zone represents the location of the tandem configured oscillating foils.**

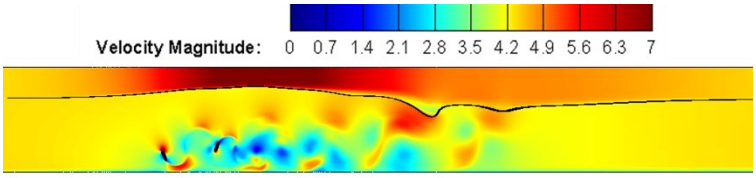


**Figure 16 Velocity contour for *D*=5*c* on *t*/*T*=2/10.**

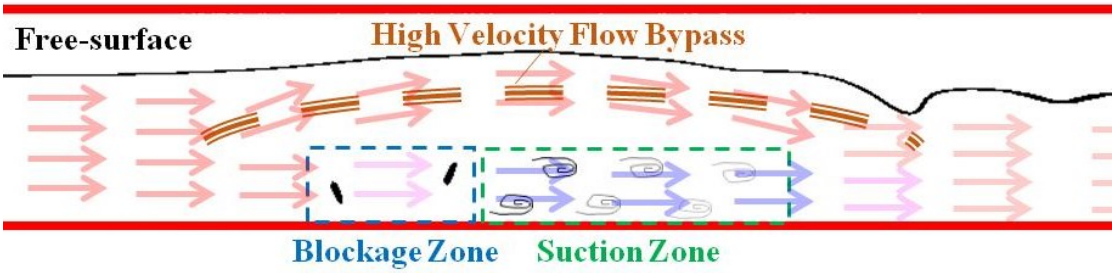


**Figure 17 Schematic plot for flow trajectory with different velocity.**